International Journal of Hydrogen Energy 60 (2024) 985–995

Contents lists available at ScienceDirect

International Journal of Hydrogen Energy

journal homepage: www.elsevier.com/locate/he

Improved conversion, selectivity, and stability during CO_2 methanation by the incorporation of Ce in Ni, Co, and Fe-hydrotalcite-derived catalysts

Carlos Mendoza-Merlano, Juan Tapia-Pérez, Efraím Serna-Galvis, Dora Hoyos-Ayala, Johana Arboleda-Echavarría, Adriana Echavarría-Isaza *

Grupo Catalizadores y Adsorbentes, Universidad de Antioquia UdeA, AA 1226, Calle 70 No. 52-21, Medellín, Colombia

ARTICLE INFO

Handling Editor: Dr A Iranzo

Keywords:
CO_2 conversion
Catalytic performance
Ceria incorporation
Hydrotalcite-derived catalysts

ABSTRACT

In this work, Ni-based mixed metal oxide (MMOs) materials were synthesized by coprecipitation, and then ceria (CeO_2) was incorporated. The obtained structures were characterized by XRD, TEM, BET, H_2-TPR, and CO_2-TPD techniques. The synthesized materials were evaluated in the CO_2 methanation process (250–400 °C range). Firstly, the effects of space velocity and Ni loading on the catalyst were tested, and 36000 h^{-1} and 5 % of Ni were found to be suitable conditions for CO_2 conversion. The addition of Co or Fe to the Ni-based MMO was then assessed. Co improved the catalytic activity, meanwhile, the Fe addition did not have an enhancing effect. Afterward, the role of CeO_2 as support on Ni-, NiFe- and NiCo-based MMOs was evaluated, evidencing that selectivity and space-time yields were enhanced in the materials by the CeO_2 presence. Furthermore, due to the characteristics of CeO_2, the MMO containing nickel, cobalt, and ceria was more stable, showing ~85% conversion of CO_2 after 1400 min of continuous use.

1. Introduction

The use of fossil fuels has enhanced global economic activity for many years. At the same time, the continuous emission of carbon dioxide (CO_2) from burning these fuels strongly affects the environment and the sustainability of the earth due to its contribution to climate change [1,2]. There are two main ways to address climate change: the decrease emissions of greenhouse gases (such as CO_2) and increase the efficient usage of alternative energy sources simultaneously [3]. In this panorama, CO_2 methanation has attracted attention because of its potential ability to decrease carbon emissions and generate methane, a fuel (or energy carrier) and a precursor for manufacturing organic products [4].

The production of methane by catalytic hydrogenation of CO_2 has been extensively studied through the Sabatier reaction (Eq. (1)), in which methane is formed by the interaction between carbon dioxide and hydrogen. The methanation process comes from the concept of power-to-gas conversion, where an excess of electric power is converted into a gaseous energy carrier (e.g., methane) by reaction with an external carbon dioxide source [4]. As mentioned above, the methanation of CO_2 is a catalytic process, and different metals have been employed in the catalytic system. There are different accepted classifications depending on the activity and selectivity of the catalysts. The order in terms of activity for representative metals in this reaction has been reported as Ru > Fe > Ni > Co > Rh > Pd > Pt while for selectivity it has been reported as Pd > Pt > Ir > Ni > Rh > Co > Fe > Ru [4].

$$CO_{2(g)} + 4H_{2(g)} \rightarrow CH_{4(g)} + 2H_2O_{(l)}\ \Delta H^0_{25} = -165\ \text{kJmol}^{-1} \quad (1)$$

Despite the excellent catalytic properties of materials whose active phase is a noble metal (e.g., Ru), these materials have disadvantages such as their high cost and low availability [5,6]. Then, catalysts based on Ni are a very attractive alternative thanks to the low cost and abundance of this metal, as well as they have elevated catalytic activity at high temperatures. Indeed, the literature offers an extensive overview of the use of Ni as an active phase in catalytic systems used for methanation reactions. Also, Ni can be supported in diverse materials for applications in the methanation process [4,7,8].

An important aspect of the hydrogenation of CO_2 is the properties that the support must provide to the catalytic systems. The influence of the active phases on the metallic dispersion is highlighted as the key factor in the activation of the CO_2 molecule. As CO_2 is considered a molecule with acid characteristics, greater activity will occur with support with basic sites [2]. Recently, hydrotalcites (HTs) have become more important as precursors of catalytic support for CO_2 conversion [3]. HTs are described as a set of sheets formed by hydroxides of

* Corresponding author.
E-mail address: adriana.echavarria@udea.edu.co (A. Echavarría-Isaza).

https://doi.org/10.1016/j.ijhydene.2024.02.149
Received 21 November 2023; Received in revised form 27 January 2024; Accepted 10 February 2024
Available online 24 February 2024

Table 1
List of synthesized hydrotalcites and their respective MMOs obtained by calcination.

Molar ratio[a]	HT abbreviation	Theoretical MMOs	MMO abbreviation
6 Mg:2Al:25H_2O	HTMgAl	$Mg_6Al_2O_9$	MMOMgAl
5 Mg:Ni:2Al:25H_2O	HTNi	$Mg_5NiAl_2O_9$	MMONi
4.5 Mg:1.5Ni:2Al:25H_2O	HTNi1.5	$Mg_{4.5}Ni_{1.5}Al_2O_9$	MMONi1.5
4 Mg:2Ni:2Al:25H_2O	HTNi2	$Mg_4Ni_2Al_2O_9$	MMONi2
4.7 Mg:Ni:0.3Co:2Al:25H_2O	HTNiCo	$Mg_{4.7}NiCo_{0.3}Al_2O_9$	MMONiCo
5 Mg:Ni:0.3Fe:1.7Al:25H_2O	HTNiFe	$Mg_5NiAl_{1.7}Fe_{0.3}O_9$	MMONiFe
OMNi:0.3Ce[EDTA]$^-$	HTNi + Ce (R)	$Mg_5NiAl_2O_9 + 0.3CeO_2$	MMONi + Ce
OMNiCo:0.3Ce[EDTA]$^-$	HTNiCo + Ce (R)	$Mg_{4.7}NiCo_{0.3}Al_2O_9 + 0.3CeO_2$	MMONiCo + Ce
OMNiFe:0.3Ce[EDTA]$^-$	HTNiFe + Ce (R)	$Mg_5NiAl_{1.7}Fe_{0.3}O_9 + 0.3CeO_2$	MMONiFe + Ce

[a] The values of the molar ratios used for the synthesis. (R): prepared by the reconstruction method.

different divalent and trivalent metals. The most common HTs have magnesium and aluminum as divalent and trivalent metals in their framework, respectively. In 1915, Manese et al. published the molecular formula of HTs, stating for the first time that carbonate ions between sheets were essential to maintain the structure [9–11]. HTs are of special interest in materials science because, upon calcination, they turn into mixed metal oxides (MMO) with basic properties, having high metal dispersion, and thermal stability [11]. Similar to MMOs derived from HTs, cerium oxide (CeO_2) can be another potential support due to its oxygen storage properties. In various catalytic systems, CeO_2 improves activity due to electronic and structural changes that increase both the metal-support interaction and metal dispersion [12–14].

In addition to the role of the support, other important aspects of catalysts to consider for CO_2 methanation are the active metal loading (i.e., the quantity of metal) and multi-composition (i.e., the presence of several active metals). These parameters influence dispersion and interaction with the support, crystallinity, surface area, and basicity, and consequently, they determine the catalytic performance [15]. It is therefore relevant to have a proper balance between the loading of active metal and the concentration of basic sites to prepare a catalyst with high activity for the methanation process. Bearing this in mind, many previous studies have reported the synthesis of Ni-based MMOs derived from HTs and their use in CO_2 conversion [2,3,16]. However, the enhancement of catalytic activity and stability in the development of catalysts for CO_2 methanation remains a challenge [2]. Thus, the present research considers the incorporation of ceria in Ni-, Co-, and Fe-hydrotalcite-derived materials, as a strategy to improve the conversion, selectivity, and stability of the catalyst in the CO_2 methanation process. It can be mentioned that a recent work deals with the methanation of carbon dioxide using ceria-supported cobalt but such a work did not consider the role of other metals (e.g., Fe), the combination of Co and Ni, or MMOs obtained from HTs [17]. Additionally, although previous literature reports the use of Co–Ni–Mg–Al mixed oxides in the methanation process, the incorporation of Ce into such MMOs is not presented therein [18]. Therefore, this lack of information about CO_2 methanation using hydrotalcite-derived catalysts is covered in our work.

The present study tested the performance of Ni-based MMO on the CO_2 methanation process by the introduction of Co, Fe, or ceria. In this work, Ni-based MMOs from HTs were synthesized and characterized, and the effect of catalyst mass and Ni loading on the material was initially assessed in the CO_2 methanation process (in the 250–400 °C range). Those initial tests provided the proper conditions of space velocity and Ni loading values to operate the methanation process. Then, the effects of a second metal addition (i.e., Co or Fe) to the Ni-based MMO on catalytic performance (i.e., CO_2 conversion and selectivity) was evaluated, and the performance was linked to the properties of the materials (e.g., reducibility and basicity). Afterward, the performance of ceria (CeO_2) as a support in Ni-, NiFe-, and NiCo-based MMOs was assessed using the reconstruction method. An improvement in the catalytic activity and the space-time yield was found due to the ceria presence. Finally, stability was tested for the two catalysts that performed best at CO_2 methanation (i.e., MMONiCo and MMONiCo + Ce). We can remark that the material containing nickel, cobalt, and ceria was the most stable, with no significant changes in the catalytic activity (i.e., high carbon dioxide conversion) after a long treatment time.

2. Materials and methods

2.1. Hydrotalcite and mixed oxide synthesis

HTs were synthesized by the coprecipitation method. Nitrates metallics such as $Mg(NO_3)_2$ (Merck, 99.3 %), $Al(NO_3)_3$ (Merck, 99.7 %), $Co(NO_3)_2{\cdot}6H_2O$ (J.T Baker, 99.3 %), $Fe(NO_3)_3{\cdot}9H_2O$ (Merck, 99.9 %) and $(NO_3)_2{\cdot}6H_2O$ (Alfa Aesar, 98.5 %), were used to the synthesis. The respective nitrates were added gradually to sodium carbonate solution (JT Baker, 99.0 %) at 65 °C, without pH change to avoid problems of the crystalline structure formation. Once the nitrates were added, the solution was stirred for 1 h and crystallized for 4 h. The resultant solid was washed until neutral pH and then dried at 90 °C for 24 h. In this way, the HTs with different compositions were obtained.

To produce the MMOs, the synthesized HTs were calcined at 500 °C for 8 h. Due to difficulties precipitating Ce in the HT synthesis, the reconstruction methodology from the MMO was used. This method is advantageous due to most of the metal remains near the surface [5], which provides special properties for applications in catalysis [6,7]. A fixed amount of $Ce(NO_3)_3{\cdot}6H_2O$ (Merck, 99.99 %) was used and complexed with EDTA solution at pH 10 to get the chemical species of Ce $[EDTA]^-$. The MMO from the HT was added to the solution (1 mol of Ce for each 3 mol of Ni) and vigorously stirred for 24 h. The resulting solid was filtered, washed, and finally dried at 80 °C for 24 h [19]. Table 1 shows the molar ratio of the hydrotalcites and, in a simplified way, their corresponding MMOs.

2.2. Characterization

The XRD patterns of the catalysts were obtained using a PANalytical Empyrean diffractometer with Cu Kα radiation (λ = 1.5404 Å). The analyses involved a time of 50 s per step and a step size of 0.05° between 5° and 80° (2θ) in the reflection configuration. The compositional analyses were carried out in a Thermo Scientific Ice 3000 atomic absorption (AA) spectrometer. The sample (50 mg) was diluted with acid (100 μL) of concentrated HNO_3 at room temperature. The resulting mixture was dissolved into 100 mL and dilutions were made for analysis.

The thermograms were obtained through the utilization of a TA Instruments TGA 5500 analyzer. The experimental procedure involved the placement of approximately 25 mg of the sample in a Pt pan, which was then positioned in an IR oven. The sample was subjected to heating at a ramp rate of 10 °C min^{-1} until it reached a temperature of 800 °C. During the heating process, an airflow of 40 mL min^{-1} was maintained. The N_2 adsorption-desorption isotherms were determined using a Micromeritics ASAP2020plus instrument. Initially, 250 mg of the sample was prepared at 350 °C for 4 h under a high vacuum to eliminate adsorbed contaminants. The specific surface area (S_{BET}) was calculated by the BET equation, which involved the relative pressure range of

Table 2
HTs structural parameter and MMOs elemental composition.

HT abbreviation	HTs		CR (%)
	Cell parameters		
	a (nm)	c (nm)	
HTNi	0.3067	2.3358	100
HTNi1.5	0.3057	2.3336	80
HTNi2	0.3054	2.3236	41
HTNiCo	0.3057	2.3262	37
HTNiFe	0.3056	2.3264	37
HTNi + Ce (R)	0.3061	2.3250	17
HTNiCo + Ce (R)	0.3061	2.2959	18
HTNiFe + Ce (R)	0.3058	2.2860	15

MMO abbreviation	MMOs			Molar ratio MMO[a]	(C^{2+}/C^{3+}) MMO[b]
	Metal(%)				
	Ni	Co	Fe		
MMONi	15.8	–	–	$Mg_{5.1}Ni_{1.0}Al_{1.8}O_{8.8}$	3.3
MMONi1.5	22.6	–	–	$Mg_{4.5}Ni_{1.5}Al_{1.9}O_{8.8}$	3.3
MMONi2	29.2	–	–	$Mg_{4.0}Ni_{2.0}Al_{1.8}O_{8.7}$	3.3
MMONiCo	15.5	4.7	–	$Mg_{4.6}Ni_{1.0}Co_{0.3}Al_{1.9}O_{8.7}$	3.1
MMONiFe	15.5	–	4.1	$Mg_{5.0}Ni_{1.0}Al_{1.6}Fe_{0.3}O_{8.8}$	3.2
MMONi + Ce	10.8	–	–	$Mg_{4.8}Ni_{0.7}Al_{2.1}O_{8.1}$+0.3$CeO_2$	2.6
MMONiCo + Ce	11.9	3.0	–	$Mg_{4.5}Ni_{0.8}Co_{0.2}Al_{1.9}O_{7.8}$+0.3$CeO_2$	2.9
MMONiFe + Ce	14.1	–	5.4	$Mg_{4.5}Ni_{1.0}Al_{1.9}Fe_{0.4}O_{8.2}$+0.3$CeO_2$	2.4

[a] Metals determined by AA.
[b] Molar ratio of divalent and trivalent cationic species.

0.01–0.1 p/p0 in a linear plot of $((p_0/p)^{-1})$ vs. p/p_0 [20]. Additionally, the total pore volume (V_{total}) was determined at the last point of p/p_0, and the t-plot method was employed to calculate the external area (S_{ext}) and micropore volume (V_{micro}). The morphology of the catalysts was examined using scanning electron microscopy (SEM) in a JEOL JSM-6490LV instrument. Transmission electron microscopy (TEM) with FEI Tecnai F20 Super-Twin TMP was employed to investigate the distribution of metal particles within the catalysts at a nanoscale level.

Energy dispersive X-ray (EDX) analyses were utilized for mapping the elemental composition present in the catalysts. X-ray photoelectron spectroscopy (XPS) tests were conducted using a SPECS® ultra-high vacuum spectrometer (UHV) to analyze the surface of the catalysts. The instrument was equipped with a 150 1D-DLD PHOIBOS® hemispherical analyzer with an angular resolution of fewer than 0.5° and a monochromatic Al X-ray source. To calibrate the spectrum binding energy positions, the C1s peak at 284.6 eV was employed as the reference value. It is important to mention that the XPS and TEM analyses were performed on the reduced samples but with low exposure to air. The temperature-programmed reduction (TPR) profiles for the catalysts were acquired using a Chemisorb 2720 unit manufactured by Micromeritics. The procedure involved placing a sample of 100 mg into a quartz reactor, followed by activation in an argon atmosphere flow at 500 °C for 1 h to eliminate contaminants. The reduction process was conducted using a 10% H_2/Ar gas mixture with a flow rate of 30 mL min^{-1} at 10 °C min^{-1} within the temperature range of 25–900 °C. The consumed hydrogen was monitored by a TCD detector. The CO_2 temperature-programmed desorption (CO_2-TPD) analyses were conducted in the Chemisorb 2720 unit. The sample (100 mg) was placed in a quartz reactor and activated in a helium atmosphere at 500 °C for 1 h. The adsorption process was carried out at 80 °C with a feed of 10% CO_2/He for 1 h. The desorption step was recorded over a temperature range from 25 to 900 °C, with a ramp of 10 °C min^{-1}. The variation of CO_2 in line was quantified using a TCD detector.

The active metal surface area of the samples was analyzed using a Chemisorb 2720 apparatus. Initially, 200 mg of the sample was reduced at 850 °C with a flow rate of 100 mL min^{-1} of a 10% H_2/Ar mixture gas for 1 h. After the reduction process, the sample was purged with 100 mL min^{-1} of Argon for 0.5 h and then allowed to return to room temperature. Subsequently, the sample was titrated with hydrogen (H_2) using a pulse of 250 μL of a 10% H_2/Ar gas mixture. The signal of H_2 was monitored using a mass spectrometer (Cirrus II), to ensure the complete saturation of the active metals on the sample. The active metal surface was determined using Eq. (2), which contains the adsorbed H_2 volume in cm^3 per gram of sample (V_{ads}), the Avogadro number (N_A: 6.023 x 10^{23} molecules mol^{-1}), the cross-sectional area of active metal (σ_m: 6.51 Å for Ni, 6.59 Å for Co, 6.09 Å for Fe) [21], stoichiometric factor (S_f: 2 atoms of Ni, Co or Fe per 1 molecule of H_2) [22], molar volume of gas at STP (Vg: 22414 cm^3 mol^{-1}) and weight percent of the active metals (%M, see Table 2).

$$\text{Active metal surface area } \left(m^2 g^{-1}\right) = \frac{V_{ads} \bullet N_A \bullet \sigma_m \bullet s_f}{V_g \bullet \%M} \quad (2)$$

2.3. Catalytic activity

The methanation reactions were performed in a fixed bed reactor with a mixture of gases with a molar ratio of $H_2/CO = 4$ in Ar balance (40 % H_2 and 10 % CO_2). The catalyst was placed in the quartz reactor and activated with 10 % H_2 at a flow of 50 mL min^{-1} at 800 °C for the materials without ceria and at 850 °C for the solids having ceria, the maximum peak reduction, with a ramp of 10 °C min^{-1} for 1 h. The system was cooled and changed to the gas mixture for the methanation reaction. The flow was set at 50 mL min^{-1} and stabilized for 30 min. The reactor was heated at a ramp of 10 °C min^{-1} at the temperatures of interest (250, 300, 350, and 400 °C) and stabilized for 30 min at each temperature. The consumption of H_2 and CO_2 was determined by analyzing the signals detected in the mass spectrometer $m/z = 2$ and 44, respectively. The quantification process was regulated by injecting a 250 μL pulse after temperature stabilization.

The CO_2 conversion was calculated using the area of CO_2 at room temperature without conversion ($A0_{CO2}$) and the area of CO_2 at the specific temperature (AT_{CO2}) as seen in Eq. (3). On the other hand, the CH_4 selectivity was calculated using the area of methane produced at the specific reaction temperature (AT_{CH4}) and the response factor between CO_2 and CH_4 (F) as seen in Eq. (4). Space-time yield (STY), which represents the number of converted CO_2 molecules to CH_4 per time (Q_{CH4}) per catalyst volume (Eq. (5)) was determined for all the catalysts [3]. This was achieved by utilizing the CO_2 molar flow per hour (Q_{CO2}), the yield to CH_4 at 350 °C (Y_{350}), and the catalyst volume in liter (V_{cat}) introduced in the reactor. To assess the catalyst stability, a time-on-stream run was conducted for 1400 min at 350 °C.

$$CO_2 \text{ Conversion } (\%) = \frac{A0_{CO2} - AT_{CO2}}{A0_{CO2}} \cdot 100 \quad (3)$$

$$CH_4 \text{ Selectivity } (\%) = \frac{AT_{CH4} \bullet F}{A0_{CO2} - AT_{CO2}} \cdot 100 \quad (4)$$

$$\text{STY } \left(\text{mol } CH_4 \text{ L}^{-1} \text{ h}^{-1}\right) = \frac{Q_{CH4}}{V_{cat}} \quad (5)$$

3. Results and discussion

3.1. Characterization of the prepared materials

3.1.1. Structural and compositional analyses

Initially, the structural and compositional characteristics of the prepared materials were established. Table 2 shows the changes in structural parameters due to the incorporation of metals in the framework of the HTs. Firstly, to verify the possibility of isomorphic substitutions, the ionic radii of the metals (0.870 Å Ce^{4+}, 0.720 Å Mg^{2+}, 0.690 Å Ni^{2+}, 0.650 Å Co^{2+}, 0.645 Å Fe^{3+}, and 0.535 Å Al^{3+}) involved in the synthesis was considered. The increase of the Ni loading on HT

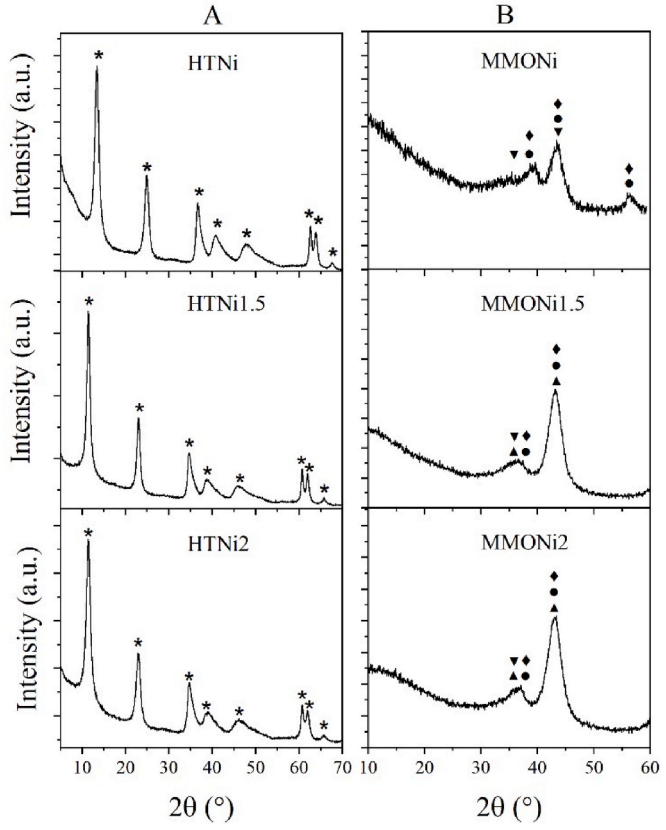

Fig. 1. XRD patterns of A) HTs. B) MMOs with different Ni loadings. (*) Hydrotalcite, (◆) $NiAl_2O_4$, (●) $MgAl_2O_4$, (▼) MgO, (▲) NiO.

caused a contraction in the unit cell volume (HTNi > HTNi1.5>HTNi2.0), especially in the laminar direction (c parameter), indicating an isomorphic substitution at the Mg^{2+} position for Ni^{2+} with smaller ionic radio. The incorporation of Co^{2+} and Fe^{3+} ions was also evidenced by the greater cell contraction concerning HTNi. However, in the reconstructed materials, there was no obvious cell expansion, indicating that the Ce metal is not substituted and probably remains on the surface [23].

From the experimental elemental composition analyses of each MMO (Table 2), the molar ratios confirmed the values calculated theoretically. The remaining di- and trivalent metal ratio is close to 3, which is expected as the precipitation was carried out at pH 10. Therefore, the only species that can stay in solution are determined by the K_{sp} of each cation [24]. The crystallinity value (CR) of the synthesized HTs diminished when the metal was incorporated into the framework. This is due to the increase in defects, resulting from the differences in ionic ratios [24]. Furthermore, the reconstructed materials showed a more drastic decrease in crystallinity (they exhibited CR values below 15–18 %, Table 2), indicating that the reconstruction would only be possible in the periphery of MMO particles and not in the total domain of the framework.

Figs. 1 and 2 contain the XRD patterns for all the synthesized materials. In Fig. 1A, the patterns of the Ni-based HTs exhibited the profiles of pure hydrotalcite for the three Ni loadings, with no visible NiO segregate impurities detected by the technique. This observation suggests that Ni has been successfully incorporated into the framework. On the other hand, Fig. 1B presents the XRD results for the MMOs, with broad peaks at $2\theta = 37.7°$, 44.0°, and 55.8°. The peaks of MMONi fit to the spinel framework of $MgAl_2O_3$ ($2\theta = 36.5°$, 44.1°, 55.0°), $NiAl_2O_4$ ($2\theta = 37.7°$, 45.3°, 55.5°), and the periclase MgO ($2\theta = 37.3°$, 42.9°), indicating that the material is a solid solution, where the Mg and Ni components coexist [3,25,26]. In the successive loading of Ni, the presence of segregate NiO phase ($2\theta = 37.3°$, 43.2°) is observed, as indicated by a shift of the peak at 44.0° towards lower angles [27].

When incorporating metals such as Fe or Co, the profile patterns show the formation of a complete hydrotalcite phase without the presence of Fe or Co oxides impurities (Fig. 2A). In turn, the MMOs containing Co and Fe exhibited the same spinel and periclase phases, indicating their incorporation into the Ni–Mg mixed oxide framework. This is supported by the absence of aggregates of Co or Fe oxides in all the patterns (Fig. 2B). On the other hand, Fig. 2C shows the XRD patterns of HTs containing Ce. The results indicate a successful reconstruction

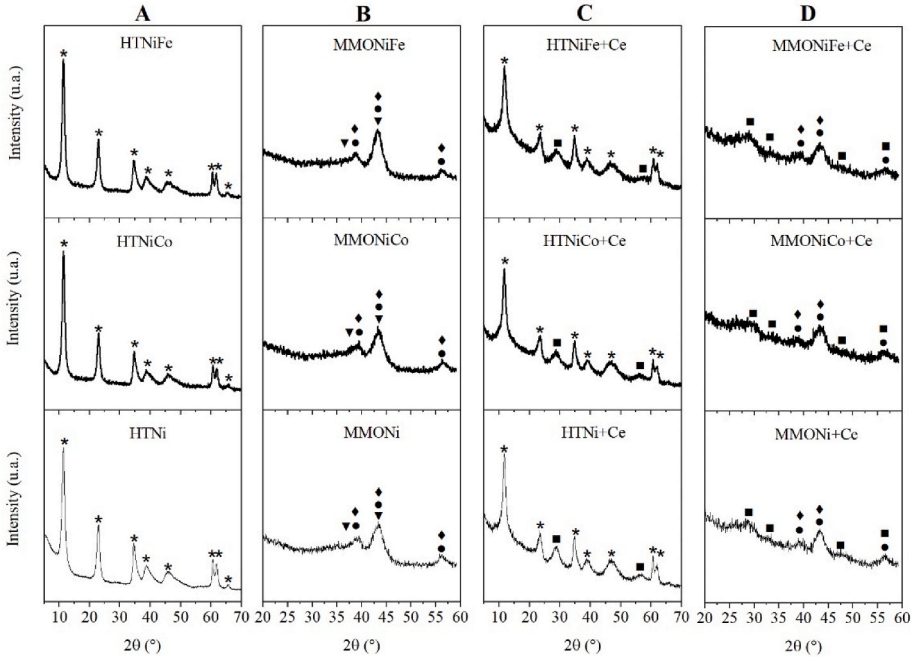

Fig. 2. XRD patterns of A) Ni, Fe, and Co HTs, B) Ni, Fe, and Co MMOs, C) Ni, Fe, and Co HTs with the addition of Ce, and D) Ni-, NiFe-, and NiCo-based MMOs with ceria. (*) Hydrotalcite, (◆) $NiAl_2O_4$, (●) $MgAl_2O_4$, (▼) MgO, (▲) NiO, (■) CeO_2.

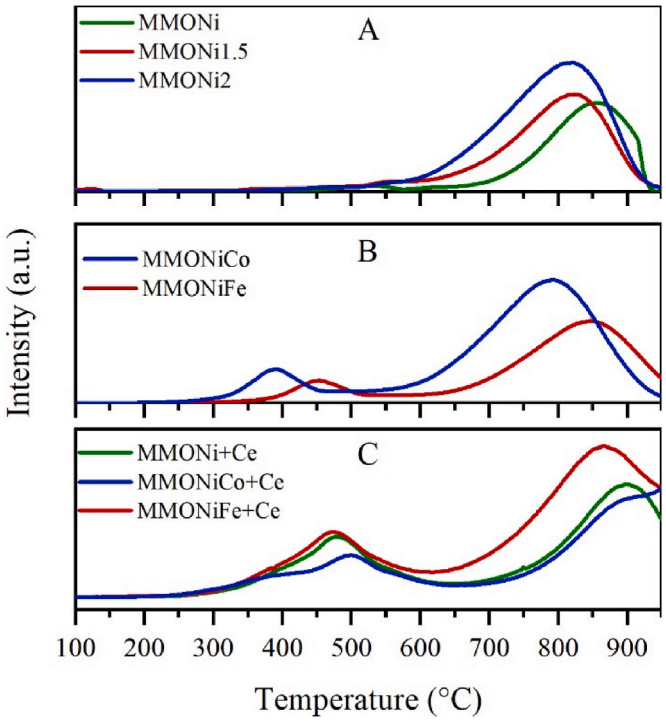

Fig. 3. H_2-TPR results for the synthesized MMOs. A) MMO with different Ni loadings, B) Effect of Co and Fe on Ni-based MMOs, and C) Effect of ceria on Ni-based MMOs.

process [28]. However, the peaks at 2θ equal to 28.6°, 33.1°, 47.5°, and 56.3° evidenced the existence of CeO_2, suggesting an extra-framework compound that is probably segregated on the solid surface [29]. Meanwhile, Fig. 2D shows the respective MMOs with the addition of ceria on the less intense peaks of MgO and Ni–Mg–Al mixed oxides. This is expected due to the amorphization and a smaller crystallite size [23].

3.1.2. Reducibility, basicity, and active metal surface area of the mixed metal oxides

The results of the H_2-TPR experiments for the MMOs obtained are presented in Fig. 3 and Table 3. From Table 3 can be noted that an increase in the Ni loading induces a higher consumption of H_2. However, the metal-reduced fractions were very similar for the MMONi at the different Ni loadings, probably due to not all the Ni particles present in the MMO is available for the reduction (i.e., at higher Ni loadings more atoms are in the core of particle than in the surface exposed to H_2). In the case of Co addition, there is no change in the metal-reduced fraction, whereas the Fe addition decreased this parameter. This could be explained by considering the oxidizing capability of these two metals. Indeed, Co is a better oxidizing agent toward H_2 than Fe [30]. In contrast, those materials containing ceria exhibited the highest metal-reduced fraction because ceria presence has a partial reduction (Eq. (6)), thus augmenting the metal-reduced fraction regarding the other materials without ceria.

Fig. 3A shows the results for the Ni-based MMOs with a first minor event at 550 °C corresponding to the reduction of NiO species coordinated with the outer layer of the MgO structure [31]. The major event was observed at 800–850 °C, and this could be associated with the reduction of NiO that is linked to the MgO lattice (i.e. in a bulk solid solution). This would explain the high-temperature reduction [3]. There was also a decrease in the maximum reduction temperatures when the nickel percentage was increased (850 °C for MMONi, 820 °C for MMONi1.5, and 815 °C for MMONi2), which is attributable to the loss of interaction with the lattice and therefore more facile reduction process [32].

As above-mentioned, the increase in the Ni loading increased H_2 consumption (Eq. (7)). Furthermore, the profile (Fig. 3A) suggests that the excess Ni mainly migrated to the inner MgO lattice due to the high calcination temperature to which the solids were subjected [33]. On the other hand, the incorporation of other metals like Co and Fe in the MMOs had a positive effect since the H_2 consumption increased in each MMO (Table 3). The incorporation of these metals promoted the appearance of peaks at temperatures between 350 and 500 °C (Fig. 3B) thanks to the partial reduction of other metallic species that had developed (Eqs. (8)–(11)) [16,34]. For MMONiCo, the minor peak at 380 °C is attributed to the reduction of Co_3O_4 to CoO (Eq. (8)), whereas for MMONiFe, the peak at 450 °C is associated with the partial reduction of Fe_2O_3 to Fe(II) species (Eq. (10)) [35,36]. The high-temperature event for MMONiCo, with a peak at 780 °C associated with the NiCoO species (Fig. 3B), showed a shift to a temperature lower than that for MMONi (Fig. 3A), which could be explained by a weakening of the interactions among the Ni–Co species and the MgO–Al_2O_3 support. In contrast, the high-temperature event for FeNi MMO occurred at 850 °C, indicating that the incorporation of Fe, especially the Fe^{3+} state, in the MMO strengthens the interaction of the NiO species with the MgO–Al_2O_3 support [37,38].

Fig. 3C presents the results of the H_2-TPR analyses for the MMOs produced from hydrotalcite reconstructed with Ce (i.e., MMONi + Ce, MMONiCo + Ce, and MMONiFe + Ce), exhibiting an increase in the intensity and reduction temperature (>850 °C) and such a high-temperature peak can be attributed to the reduction of bulk CeO_2 [39]. This reinforces the strong metal-support interaction among Ni, Co, and Fe to CeO_2. Moreover, these materials had two peaks at 380 and 480 °C (which are absent in MMONi, Fig. 3A), belonging to the surface and partial reduction of ceria underneath the surface (Eq. (6)), respectively. The signals increase and overlap with the most oxidized species of Co and Fe in MMONiCo + Ce and MMONiFe + Ce, respectively [40,41]. Therefore, the ceria support contributes to the reducibility capacity at

Table 3
Hydrogen consumption of mixed oxides and basicity.

MMOs	H_2 consumption (mmol g^{-1})	Metal-reduced fraction[a]	Active metal surface area (m^2 g^{-1})	BET surface area (m^2 g^{-1})	Basicity			
					Total (mmol g^{-1})	Weak (%)	Medium (%)	Strong (%)
MMONi	2.4	0.56	11.8	218	0.54	24	28	48
MMONi1.5	3.5	0.55	11.1	245	0.44	25	30	45
MMONi2	4.6	0.54	13.8	235	0.45	25	37	37
MMONiCo	3.2	0.54	11.3	235	0.50	19	31	49
MMONiFe	3.6	0.46	0.1	245	0.36	30	43	28
MMONi + Ce	1.5	0.61	4.9	160	0.52	4	47	49
MMONiCo + Ce	2.0	0.63	5.3	192	0.55	3	41	55
MMONiFe + Ce	2.4	0.69	0.0	200	0.52	18	19	63

[a] For the metal-reduced fraction calculation, it was assumed that 1 mol of H_2 requires 2 mol of metal.

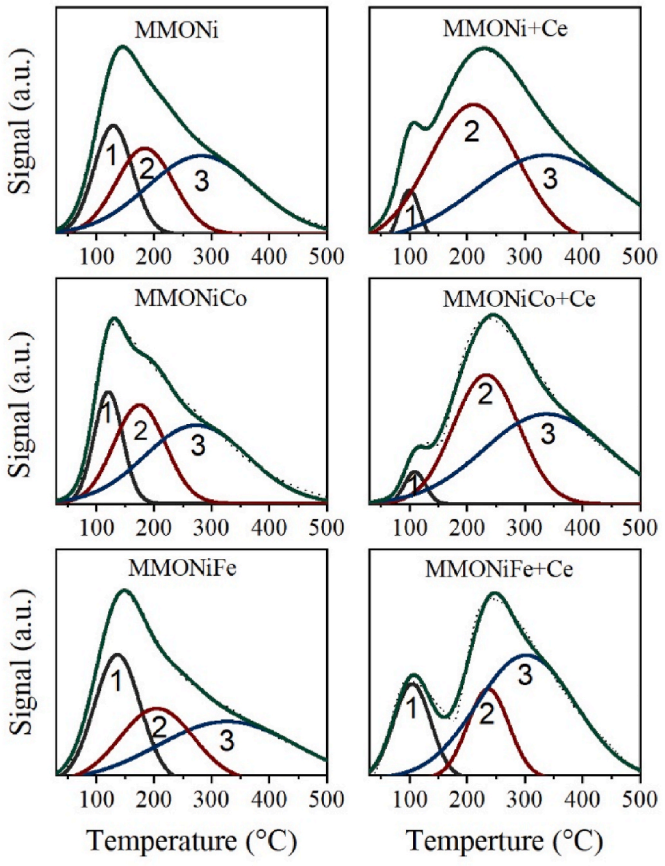

Fig. 4. CO_2-TPD of the MMOs. Basicity (1): weak, (2): medium, and (3): strong basic sites.

Table 4
XPS quantification of the species on the surface and the exposed Ni^0/Ni^{2+} ratio.

MMOs	Mg (%)	Al (%)	Ni (%)	M (%)	Ce (%)	R (Ni^0/ Ni^{2+})
MMONi	1.22	28.60	0.25		–	1.61
MMONiCo	1.04	30.51	0.28	0.19	–	1.55
MMONiFe	1.17	26.11	0.12	–	–	1.46
MMONi + Ce	1.19	22.06	0.24	–	0.14	1.25
MMONiCo + Ce	1.22	27.95	0.22	0.09	0.15	1.56
MMONiFe + Ce	1.14	21.15	0.09		0.12	–

low temperatures of the synthesized catalysts.

$$CeO_2 + yH_2 \rightarrow CeO_{2-y} + yH_2O \quad (6)$$

$$NiO + H_2 \rightarrow Ni + H_2O \quad (7)$$

$$Co_3O_4 + H_2 \rightarrow CoO + H_2O \quad (8)$$

$$CoO + H_2 \rightarrow Co + H_2O \quad (9)$$

$$Fe_2O_3 + H_2 \rightarrow 2FeO + H_2O \quad (10)$$

$$FeO + H_2 \rightarrow Fe + H_2O \quad (11)$$

The basicity strength was measured by the TPD of CO_2. In general, all the MMOs evidenced three types of basic sites from the deconvolution, as shown in Fig. 4. The first site has a weak nature at 100 °C associated with the basic OH-group on the surface, followed by the medium site at 200 °C linked to the bidentate carbonates, involving the metal–oxygen pairs [3]. The third basic site is strong, related to monodentate

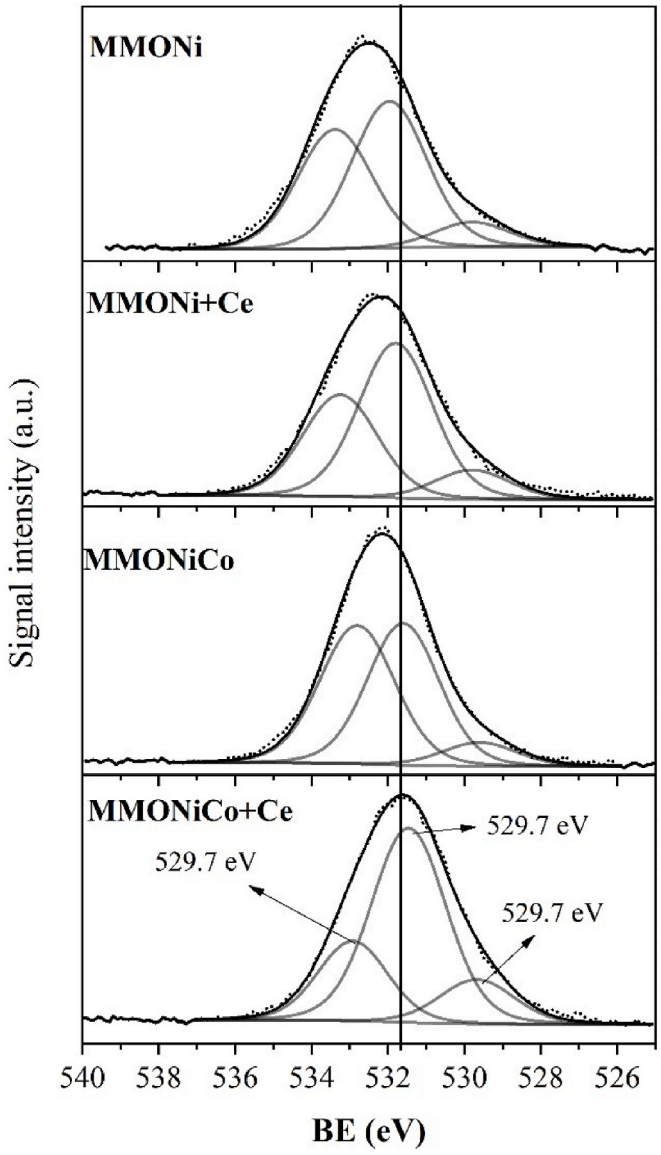

Fig. 5. O1s X-photoelectron spectra for the MMOs based on Ni and NiCo, and doped with ceria.

carbonates coming from oxygen anions of low-coordination. Also, there was a decrease in the total basicity with an increase in Ni loading, mainly representing a systematic depletion in the strong basic sites.

The addition of Co did not result in a significant change compared to MMONi, especially with the medium and strong acid sites. Therefore, the performance of catalysis when based on the alkalinity features would be the same. On the other hand, the incorporation of Fe resulted in significant depletion at strong basic sites, as fewer free oxygen pairs were available with Fe (III) species in the MgO lattice, probably leading to poor catalytic activity. Furthermore, an increase in the medium and strong basic sites was seen when ceria was added to the MMOs. Meanwhile, CeO_2 is not basic itself, as reported in the literature where CO_2 desorption remains below 200 °C [42,43]. We propose that CeO_2 stimulates the medium and strong basicity of the MMO (Table 3) that came from a reconstructed HT. The reconstruction process increased the defects and therefore resulted in low coordination in the oxygen. Moreover, the oxygen mobility coming from the redox characteristics of Ce strengthens the oxyphilic characteristics [42–44].

The data in Table 3 shows an increase in the surface area in the MMOs as the amount of Ni added to the HT increased. This could be due

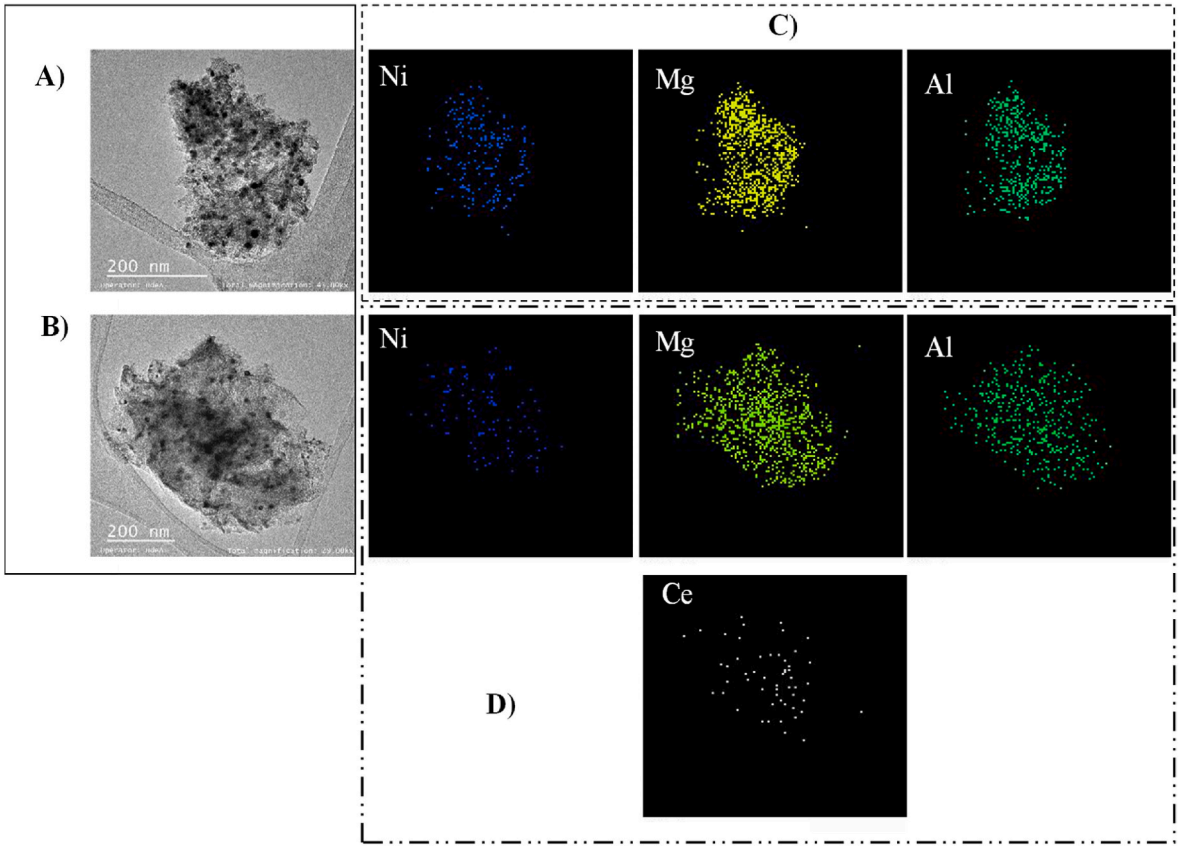

Fig. 6. TEM of the samples, A) MMONi and B) MMONi + Ce. Mapping of metals in the samples, C) MMONi and D) MMONi + Ce.

to a decrease in the crystallite size of the materials, as also shown by the unit cell contraction. The same trend appears when incorporating both Fe and Co [45]. However, as seen above, in the structure of the reconstructed hydrotalcites, the incorporation of Ce was not completed, causing the respective mixed oxide to lose some surface area. Table 3 also depicts the active metal surface area, which could provide information about the catalytic behavior. Metal surface area is linked to the number of active metal sites that can be found on the surface of the solid material (Ni, Co, and Fe). As shown in Table 3, the MMOs based on Ni show a metal surface area of between 11.1 and 13.8 $m^2\ g^{-1}$. The amount of Ni did not increase the metal surface area significantly probably because the increase of Ni leads to a decrease in the metal dispersion [46]. Therefore, an increase in the Ni loading is not a recommended strategy to improve catalysis. Meanwhile, the materials that contained Co retain the metal surface area at 11.3 $m^2\ g^{-1}$ as MMONi, which would indicate that any change in catalysis would be related to other properties more than the metal surface area. In turn, the materials containing Fe presented an undetectable metal surface area by the analytical technique. At the same time, the results suggest that the incorporation of Fe in this ratio had no synergy with Ni to chemisorb H_2 likely due to the high oxidation state of iron on the surface. In the same way, a decrease in the metal surface area was observed when incorporating Ce in the material structure, which agrees with the high energy/temperature required to reduce these MMOs [16,34].

3.1.3. XPS and TEM analyses

Table 2 shows the molar ratios of the solids that represent the chemical composition of bulk materials. However, there are significant differences when compared with the values obtained from the surface analysis performed by XPS (Table 4). It can be noted that the Ni and Mg species change significantly, which migrate to the bulk leaving a high proportion of Al on the surface of materials. The highest surface stability was therefore related to aluminum on the surface. Even so, high basicity values were found with a lower-than-expected proportion of Mg. Moreover, it is possible that the high reduction temperatures also favor the migration of these species to the bulk of the solid, as previously shown by other authors [47–49].

The solid materials were not completely reduced. However, the Ni^0/Ni^{2+} ratio is greater than 1, which indicates that a high proportion of Ni has been reduced and, as previously shown for the MMOs containing Fe and Ni, this reduction was not observed on the surface. Although the Ni^0/Ni^{2+} ratio can be misleading because the reduction process and equipment placement involve short periods of exposure to the air, the high ratio indicates that most of the Ni was reduced. Nevertheless, it is difficult and risky to look for correlations that somehow explain the ratio of metallic nickel to divalent nickel.

Another important aspect to consider is the surface oxygen of the analyzed oxides. Fig. 5 shows the three oxygen species that refer to bulk oxygens (O^{2-}), surface oxygens that give an idea of the species bound to the metal surface, and hydroxylated oxygen species (OH), with values of 529.7 eV, 531.5 eV, and 532.9 eV, respectively [47]. The bulk oxygen is of great importance due to the basicity generated by the Lewis basic sites. On the other hand, the metallic oxygen is related to surface aluminum, as shown in Table 4. However, there may also be contributions from other metals such as Mg, Ni, and Ce. Finally, the oxygen associated with hydroxylated species refers to the water adsorbed onto the surface. Although the solids were previously reduced, the contact with the environment promotes water getting adsorbed onto them.

Figs. 6 and 7 show the TEM analyses for the reduced forms of MMOs. Fig. 6 shows the mapping of the most important elements, Al(green), Mg (yellow), Ni(blue), and Ce(white), indicating a good atom distribution and the presence of Ce and Ni as the species of interest. In turn, Fig. 7 presents the size of the metallic distribution, where the effect of the second metal and the addition of Ce can be observed. The addition of Fe

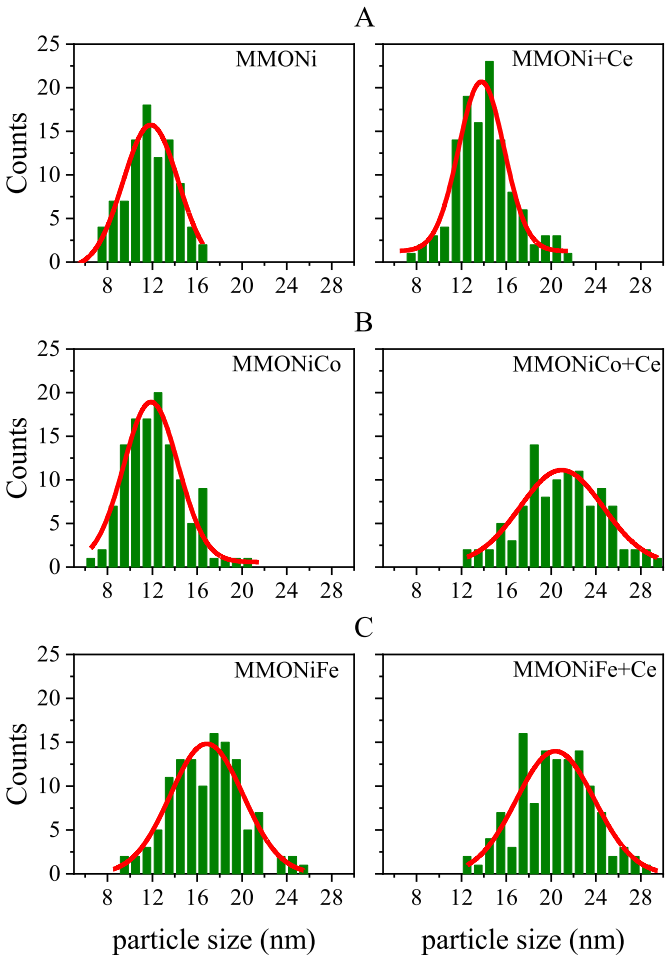

Fig. 7. Metal particle size distribution of the MMOs analyzed by TEM (minimum 100 particles counted). A) Ni, B) Ni–Co, and C) Ni–Fe.

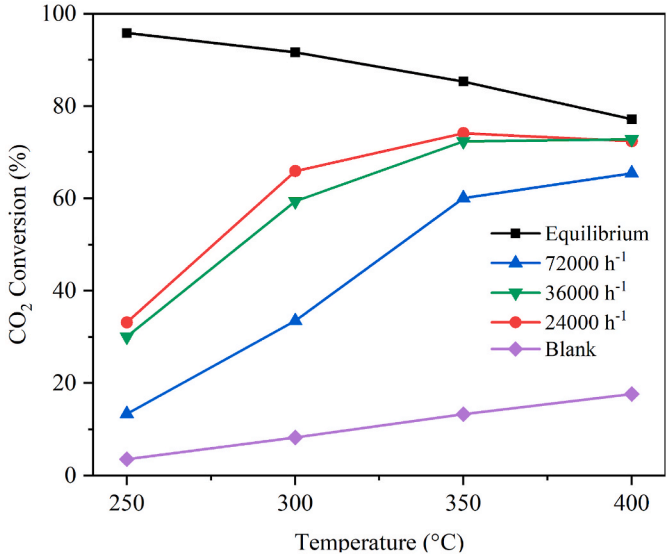

Fig. 8. Effect of catalyst mass (space velocity) on the methanation reaction profiles for MMONi.

causes a particle size increase, except in the case of cobalt where no effect was detected. However, for all catalysts that have Ce, there was an increase in the average metallic particle size, which can be explained by the high reduction temperatures to which the Ce catalyst was subjected (Fig. 3).

3.2. Catalytic activity of the materials in the methanation reaction

3.2.1. Impact of the catalyst mass and amount of Ni on the catalytic activity

The catalytic activity for the synthesized MMOs based on Ni was evaluated as a function of the temperature, also considering the impact of the catalyst mass on the reaction. Fig. 8 depicts the control experiments/systems (equilibrium and blank) and the reaction profiles at different masses of MMONi (i.e., different space velocities). The thermodynamic equilibrium profile is also shown as a reference for the maximum conversion values that can be obtained at atmospheric pressure [50]. In the blank reaction, which was carried out only with quartz wool and the Mg and Al-based mixed metal oxides, a low conversion was observed. There was no production of methane due to the absence of metal. In turn, for the catalyst at different space velocities, 20 mg of MMONi (space velocity: 72000 h^{-1}) was not enough to properly develop the reaction. It should be noted that the increase in the catalyst mass from 20 mg (72000 h^{-1}) to 40 mg (36000 h^{-1}) enhanced the conversion of CO_2. However, when the catalyst mass was raised from 40 mg (36000 h^{-1}) to 60 mg (24000 h^{-1}), no significant differences were found at the maximum conversion temperature (i.e., 350 °C, Fig. 8). Therefore, 36000 h^{-1} was used as a fixed value in all future reactions. At high space velocity, the catalyst bed could have been very short to provide enough contact time between the mixture of reacting gas and the catalyst, affecting the catalytic activity. These results are similar to those obtained by other authors [18].

As shown in Fig. 8, the increase in temperature led to higher CO_2 conversion percentages. The temperature increase induces higher interactions/collisions among the reactants and catalyst, favoring the process performance (i.e., kinetic aspect) [51]. However, the catalytic activities decrease at temperatures over 350 °C because a thermodynamic limitation in the form of a reverse water–gas shift (RWGS) reaction (Eq. (12)) becomes more favorable [1,3,52] and thus decreases the conversion of CO_2. At the same time, higher catalyst mass (which determines the space velocity) induced a high CO_2 conversion because more catalytic sites were provided to the reaction system [53]. Nevertheless, a very high catalyst mass (such as in the case of 60 mg of MMONi) did not improve the performance of the process, possibly because an excess of the catalyst provided many non-used active sites. At 60 mg of MMONi, there was no enhancement of CO_2 conversion. Considering the results in Figs. 8 and 40 mg of catalyst (i.e., 36000 h^{-1}) was used as a fixed value to continue the research.

$$CO_{2(g)} + H_{2(g)} \rightarrow CO_{(g)} + 2H_2O_{(g)} \quad \Delta H^0_{25} = 41 \text{ kJmol}^{-1} \tag{12}$$

After evaluating the effect of space velocity on the reaction of methanation, the role of the Ni loading in the catalytic performance was assessed. Fig. 9A shows the profiles of reaction for solids with different Ni loadings (MMONi, MMONi1.5, and MMONi2) prepared at different temperatures. It can be observed that the catalytic activities of these materials were moderate at 250 °C (lower than 40% of conversion), suggesting that the methanation reaction began slowly. Moreover, for the three catalysts, the maximum CO_2 conversion was obtained between 350 °C and 400 °C. This demonstrates that the Ni-based MMOs induced CO_2 methanation at lower temperatures. Such behavior was similar to the results reported for other NiMgAl-mixed oxides derived from hydrotalcite [3].

The results in Fig. 9A also revealed a decrease in catalytic performance when the percentage of Ni was increased from 10 % to 20 % (which corresponded to MMONi1.5 and MMONi2.0, respectively). The loading of metal on a supported catalyst strongly modifies its dispersion and interaction with the support, which in turn affects the catalytic performance. In general, the lower the loading of metal, the greater its

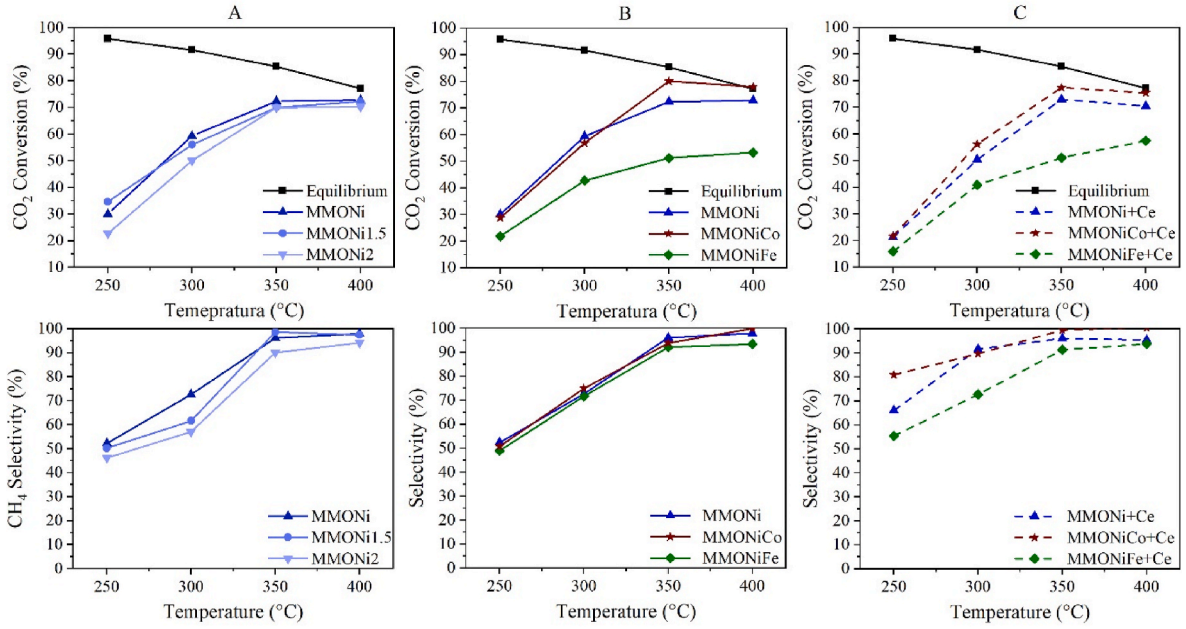

Fig. 9. Methanation reaction profiles for different MMOs based on Ni, Mg, Al, Co, Fe, and Ce. A) MMO with different Ni loading B) Effect of Co and Fe on MMO and C) MMO with the addition of ceria.

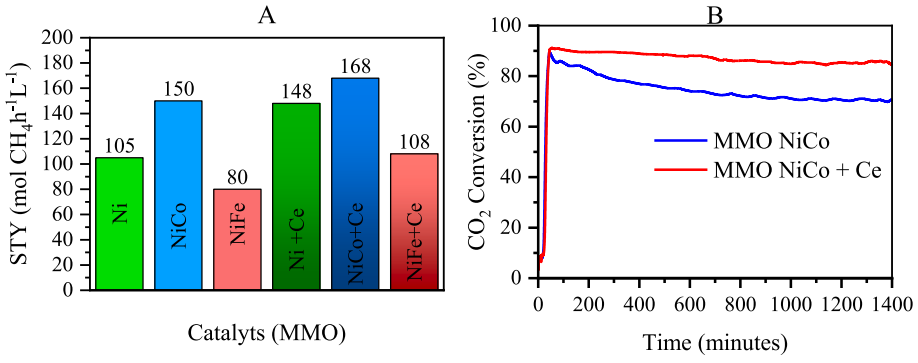

Fig. 10. Extent of the catalytic process. **A.** STY of the prepared materials. **B.** Stability test for the two best catalysts.

dispersion, and vice versa [15]. Furthermore, it is important to note that the increase in the Ni loading diminished the total basicity of the catalyst (as shown in Table 3), which worsened the adsorption of CO_2 and its subsequent conversion and selectivity. Moreover, the decrease in catalytic performance could be associated with a loss of active sites due to the Ni sintering at high reduction temperatures. These results were consistent with the literature, considering that MMONi (which has 10 % of Ni doping) exhibited the best catalytic performance (Fig. 9A). Previous studies have shown that a specific Ni doping of 5–10 % is ideal for obtaining good reactivity on the catalyst [15]. Thus, it can be concluded that the combined effects of Ni loading, and basic sites determine the catalytic activity of the prepared material [3].

3.2.2. *Effect of adding Co, Ce, and Fe to the MMONi structure*

The catalytic activity and dispersion of the active metal can be tuned via the addition of a second metal component [1]. The effect of the modification of MMONi by the addition of cobalt or iron was therefore assessed. Fig. 9B shows the results for catalytic methanation using MMONiCo and MMONiFe. The material containing Co experienced better CO_2 conversions (~80 % at 350 °C) than that containing Fe (50 % at 350 °C). The presence of cobalt improved the reactivity for the conversion of carbon dioxide into methane. Indeed, MMONiCo had a higher hydrogen consumption and CO_2 adsorption than MMONi but a similar basicity (Table 3), probably due to the high reducibility of cobalt [54]. On the contrary, the worst catalytic activity was for MMONiFe, possibly due to its low CO_2-chemisorption capability, as evidenced by having the lowest basicity (Table 4). Furthermore, Fe-doping decreased the metal surface area, blocking the availability of Ni species. In fact, the low reducibility of Fe^{3+} species could have affected Ni species on the surface of the material, thus altering the catalytic performance. The role of each metal depends on its loading, and it may be beneficial to adjust the amount of Fe in the catalyst [36,55].

The effect of incorporating CeO_2 into MMONiCo, MMONiFe, and MMONi on catalytic activity was also studied. Fig. 9C presents the results for all the ceria-containing materials. No significant differences were observed in terms of CO_2 conversion between the catalysts containing CeO_2 (i.e., MMONiFe + Ce, MMONiCo + Ce, and MMONi + Ce) and the catalysts without CeO_2 (i.e., MMONiFe, MMONiCo, and MMONi). Interestingly, a substantial improvement can be observed in selectivity to methane for MMONiCo + Ce and MMONi + Ce, especially at low temperatures. The latter results indicate a greater activation of CO_2 when CeO_2 coexists on the catalyst surface [56]. It should be noted that the presence of ceria in the catalyst enhanced the total basicity (and consequently the CO_2 chemisorption) of MMONiFe + Ce, MMONiCo + Ce, and MMONi + Ce regarding their corresponding materials without CeO_2. However, the consumption of H_2 and metal surface area of the

MMONiFe + Ce catalyst was the lowest (Table 3), explaining its worse performance (Fig. 9C) despite the presence of ceria. The improvement in selectivity to methane for MMONiCo + Ce and MMONi + Ce at low temperatures can be linked to how ceria helps to reduce the catalysts (as demonstrated in section 3.1.2.) and CO_2 adsorption, thereby, limiting the formation of coke (Eqs. (13)–(15) [1]) and favoring the generation of methane, as suggested by previous works [57,58]. However, experimental research to determine coke deposits, on the catalysts tested for the CO_2 methanation, should be performed in future works.

$$CO_2 + 2H_2 \rightarrow C + 2H_2O \quad (13)$$

$$2CO + 2H_2 \rightarrow 2C + 2H_2O \quad (14)$$

$$CH_4 \rightarrow C + 2H_2 \quad (15)$$

3.2.3. Extent of the process: yield and stability of the best MMO

The space-time yield (STY), which is a measurement of the catalytic activity yield of the materials, and represents the number of converted CO_2 molecules to CH_4 per volume of catalyst per unit of time [59,60], was calculated and presented in Fig. 10A. The SYT values followed the order MMONiCo + Ce (168 mol CH_4 h^{-1} L^{-1}) > MMONiCo (150 mol CH_4 h^{-1} L^{-1}) > MMONi + Ce (148 mol CH_4 h^{-1} L^{-1}) > MMONiFe + Ce (108 mol CH_4 h^{-1} L^{-1}) > OMNi (105 mol CH_4 h^{-1} L^{-1}) > MMONiFe (80 mol CH_4 h^{-1} L^{-1}). These STY values show that the materials containing both cobalt and ceria have a high catalytic activity yield. Furthermore, the comparison of our catalysts with the other materials used for methanation reveals that MMONiCo + Ce and MMONiCo have a higher STY than diverse Ni-based MMO catalysts (STY range: 1.8–137 mol CH_4 h^{-1} L^{-1}) [60].

The stability (also called a time-on-stream, TOS run [3]) was also evaluated for the two materials with the best catalytic performance (i.e., MMONiCo + Ce and MMONiCo). Fig. 10B depicts the CO_2 conversion at 350 °C for 1400 min. The TOS run fitted well with the previous catalytic performances for such materials (Fig. 9B), exhibiting CO_2 conversions higher than 80 % even after 1400 min. Remarkably MMONiCo + Ce remained more stable than MMONiCo with no significant changes in catalytic activity (~85 % of CO_2 conversion after 1400 min of continuous use). Hence, it can be concluded that ceria improved both the catalytic activity and stability of the MMONiCo catalyst. Also, it was observed that our MMONiCo + Ce material had a similar stability behavior compared to other NiCo-HT-derived catalysts previously reported in the literature [18].

4. Conclusions

Ni-based MMOs were effectively synthesized from HTs and then characterized. The MMONi materials efficiently promoted CO_2 methanation at low temperatures (350–400 °C) and a high space velocity (36000 h^{-1}). However, an excess of Ni loading (e.g., >10 %) had a detrimental effect on the catalytic performance due to its effect on metal dispersion and interaction with the support, and the fact that it diminished the basicity of the catalyst. The addition of a second active metal such as Co or Fe modified the activity of the catalyst. The presence of iron (i.e., MMONiFe material) affected the conversion of CO_2, probably because it is hard to reduce and has lower basicity, and due to the decrease in the metal surface area. In contrast, Co had a positive effect as it enhanced catalytic activity because its high reducibility favored H_2 consumption. It was possible to successfully incorporate ceria (CeO_2) in Ni-based and NiCo-based MMOs by using the reconstruction method. The incorporation of ceria as a support improved the selectivity toward methane at low temperatures (250–350 °C) and this led to a greater extent of the process when CeO_2 was present and MMONi had Co as a dopant. Indeed, the STY results suggest that the material containing nickel, cobalt, and ceria (i.e., MMONiCo + Ce) converts the CO_2 into CH_4 molecules very efficiently. This can be linked to the fact that ceria greatly helps to reduce the catalysts and has a higher basicity and metal surface area. Additionally, the MMONiCo + Ce material showed high stability, achieving elevated CO_2 conversion (~85 %) even after 1400 min of continuous use.

Declaration of competing interest

The authors declare that they have no known competing financial interests or personal relationships that could have appeared to influence the work reported in this paper.

Acknowledgments

The authors gratefully acknowledge the financial support provided by the Colombia Scientific Program within the framework of the call Ecosistema Científico (Contract No. FP44842- 218–2018).

References

[1] Liu Z, Gao X, Liu B, Ma Q, Zhao T sheng, Zhang J. Recent advances in thermal catalytic CO_2 methanation on hydrotalcite-derived catalysts. Fuel 2022;321:124115. https://doi.org/10.1016/j.fuel.2022.124115.
[2] Huynh HL, Yu Z. CO_2 methanation on hydrotalcite-derived catalysts and structured reactors: A review. Energy Technol 2020;8:1901475. https://doi.org/10.1002/ente.201901475.
[3] Nguyen-Quang M, Azzolina-Jury F, Samojeden B, Motak M, Da Costa P. On the influence of the preparation routes of NiMgAl-mixed oxides derived from hydrotalcite on their CO_2 methanation catalytic activities. Int J Hydrogen Energy 2022;47:37783–91. https://doi.org/10.1016/j.ijhydene.2022.08.278.
[4] Lee WJ, Li C, Prajitno H, Yoo J, Patel J, Yang Y, et al. Recent trend in thermal catalytic low temperature CO_2 methanation: zz critical review. Catal Today 2021;368:2–19. https://doi.org/10.1016/j.cattod.2020.02.017.
[5] Sharma S, Hu Z, Zhang P, McFarland EW, Metiu H. CO_2 methanation on Ru-doped ceria. J Catal 2011;278:297–309. https://doi.org/10.1016/j.jcat.2010.12.015.
[6] Janke C, Duyar MS, Hoskins M, Farrauto R. Catalytic and adsorption studies for the hydrogenation of CO_2 to methane. Appl Catal B Environ 2014;152–153:184–91. https://doi.org/10.1016/j.apcatb.2014.01.016.
[7] Frontera P, Macario A, Ferraro M, Antonucci PL. Supported catalysts for CO_2 methanation: a review. Catalysts 2017;7:1–28. https://doi.org/10.3390/catal7020059.
[8] Su X, Xu J, Liang B, Duan H, Hou B, Huang Y. Catalytic carbon dioxide hydrogenation to methane: a review of recent studies. J Energy Chem 2016;25:553–65. https://doi.org/10.1016/j.jechem.2016.03.009.
[9] Manasse E. Sulla composizione chimica delle terre gialle e bolari del Monte Amiata. Atti Della Soc Toscana Di Sci Nat Resid Pisa Mem 1915;30:101.
[10] Corma A, Fornés V, Rey F. Hydrotalcites as base catalysts: Influence of the chemical composition and synthesis conditions on the dehydrogenation of isopropanol. J Catal 1994;148:205–12. https://doi.org/10.1006/jcat.1994.1202.
[11] Centi G, Perathoner S. Catalysis by layered materials: a review. Microporous Mesoporous Mater 2008;107:3–15. https://doi.org/10.1016/j.micromeso.2007.03.011.
[12] Trovarelli A, Deleitenburg C, Dolcetti G, Lorca JL. CO_2 methanation under transient and steady-state conditions over Rh/CeO_2 and CeO_2-promoted Rh/SiO_2: The Role of Surface and Bulk Ceria. J Catal 1995;151:111–24. https://doi.org/10.1006/jcat.1995.1014.
[13] Liu H, Zou X, Wang X, Lu X, Ding W. Effect of CeO_2 addition on Ni/Al_2O_3 catalysts for methanation of carbon dioxide with hydrogen. J Nat Gas Chem 2012;21:703–7. https://doi.org/10.1016/S1003-9953(11)60422-2.
[14] Rahmani S, Rezaei M, Meshkani F. Preparation of promoted nickel catalysts supported on mesoporous nanocrystalline gamma alumina for carbon dioxide methanation reaction. J Ind Eng Chem 2014;20:4176–82. https://doi.org/10.1016/j.jiec.2014.01.017.
[15] Aziz MAA, Jalil AA, Triwahyono S, Saad MWA. CO_2 methanation over Ni-promoted mesostructured silica nanoparticles: Influence of Ni loading and water vapor on activity and response surface methodology studies. Chem Eng J 2015;260:757–64. https://doi.org/10.1016/j.cej.2014.09.031.
[16] Mebrahtu C, Krebs F, Perathoner S, Abate S, Centi G, Palkovits R. Hydrotalcite based Ni–Fe/(Mg, Al)Ox catalysts for CO_2 methanation – tailoring Fe content for improved CO dissociation, basicity, and particle size. Catal Sci Technol 2018;8:1016–27. https://doi.org/10.1039/C7CY02099F.
[17] Struijs JJC, Muravev V, Verheijen MA, Hensen EJM, Kosinov N. ceria-supported cobalt catalyst for low-temperature methanation at low partial pressures of CO_2. Angew Chem Int Ed 2023;62. https://doi.org/10.1002/anie.202214864.
[18] Summa P, Świrk Da Costa K, Gopakumar J, Samojeden B, Motak M, Rønning M, et al. Optimization of Co-Ni-Mg-Al mixed-oxides CO_2 methanation catalysts with solution combustion synthesis: on the importance of Co incorporation and basicity. Appl Mater Today 2023;32:101795. https://doi.org/10.1016/j.apmt.2023.101795.
[19] Tsyganok AI, Inaba M, Tsunoda T, Uchida K, Suzuki K, Takehira K, et al. Rational design of Mg-Al mixed oxide-supported bimetallic catalysts for dry reforming of

methane. Appl Catal Gen 2005;292:328–43. https://doi.org/10.1016/j.apcata.2005.06.007.
[20] Osterrieth JWM, Rampersad J, Madden D, Rampal N, Skoric L, Connolly B, et al. How reproducible are surface areas calculated from the BET equation? Adv Mater 2022;34. https://doi.org/10.1002/adma.202201502.
[21] Bergeret G, Gallezot P. Particle size and dispersion measurements. Handb. Heterog. Catal., Wiley 2008:738–65. https://doi.org/10.1002/9783527610044.hetcat0038.
[22] Gil A. Classical and new insights into the methodology for characterizing adsorbents and metal catalysts by chemical adsorption. Catal Today 2023;423:114016. https://doi.org/10.1016/j.cattod.2023.01.023.
[23] Daza CE, Gallego J, Mondragón F, Moreno S, Molina R. High stability of Ce-promoted Ni/Mg-Al catalysts derived from hydrotalcites in dry reforming of methane. Fuel 2010;89:592–603. https://doi.org/10.1016/j.fuel.2009.10.010.
[24] Tsyganok A, Sayari A. Incorporation of transition metals into Mg-Al layered double hydroxides: Coprecipitation of cations vs. their pre-complexation with an anionic chelator. J Solid State Chem 2006;179:1830–41. https://doi.org/10.1016/j.jssc.2006.03.029.
[25] Seo B, Ko EH, Boo J, Kim M, Kang D, Park N. CO_2 hydrogenation on $Ni_xMg_1-xAl_2O_4$: a comparative study of MgAl2O4 and NiAl2O4. Catalysts 2021;11:1026. https://doi.org/10.3390/catal11091026.
[26] Portillo Crespo MA, Vidal-Barrero F, Azancot L, Reina TR, Campoy M. Insights on guerbet reaction: production of biobutanol from bioethanol over a Mg–Al spinel catalyst. Front Chem 2022;10:1–10. https://doi.org/10.3389/fchem.2022.945596.
[27] Maniammal K, Madhu G, Biju V. X-ray diffraction line profile analysis of nanostructured nickel oxide: shape factor and convolution of crystallite size and microstrain contributions. Phys E Low-Dimensional Syst Nanostructures 2017;85:214–22. https://doi.org/10.1016/j.physe.2016.08.035.
[28] Coumans FJAG, Mitchell S, Schütz J, Medlock J, Pérez-Ramírez J. Hydrotalcite-derived mixed oxides for the synthesis of a key vitamin a intermediate reducing waste. ACS Omega 2018;3:15293–301. https://doi.org/10.1021/acsomega.8b02234.
[29] Michalska M, Lemański K, Sikora A. Spectroscopic and structural properties of CeO_2 nanocrystals doped with La^{3+}, Nd^{3+} and modified on their surface with Ag nanoparticles. Heliyon 2021;7:e06958. https://doi.org/10.1016/j.heliyon.2021.e06958.
[30] Vanýsek P. Electrochemical series. In: Lide DR, editor. CRC handb. Chem. Phys.. 84th ed. CRC Press; 2004. p. 8–21.
[31] Summa P, Świrk K, Wierzbicki D, Motak M, Alxneit I, Rønning M, et al. Co-precipitated Ni-Mg-Al hydrotalcite-derived catalyst promoted with vanadium for CO_2 methanation. Molecules 2021;26. https://doi.org/10.3390/molecules26216506.
[32] Zhang Z, Tian Y, Zhang L, Hu S, Xiang J, Wang Y, et al. Impacts of nickel loading on properties, catalytic behaviors of Ni/Γ–Al_2O_3 catalysts and the reaction intermediates formed in methanation of CO_2. Int J Hydrogen Energy 2019;44:9291–306. https://doi.org/10.1016/j.ijhydene.2019.02.129.
[33] Parmaliana A, Arena F, Frusteri F, Giordano N. Temperature-programmed reduction study of NiO–MgO interactions in magnesia-supported Ni catalysts and NiO–MgO physical mixture. J Chem Soc Faraday Trans 1990;86:2663–9. https://doi.org/10.1039/FT9908602663.
[34] Summa P, Świrk K, Wang Y, Samojeden B, Rønning M, Hu C, et al. Effect of cobalt promotion on hydrotalcite-derived nickel catalyst for CO_2 methanation. Appl Mater Today 2021;25:101211. https://doi.org/10.1016/j.apmt.2021.101211.
[35] Mountapmbeme Kouotou P, Waqas M, El Kasmi A, Atour Z, Tian Z-Y. Influence of Co addition on Ni-Co mixed oxide catalysts toward the deep oxidation of low-rank unsaturated hydrocarbons. Appl Catal Gen 2021;612:117990. https://doi.org/10.1016/j.apcata.2021.117990.
[36] Yin L, Chen X, Sun M, Zhao B, Chen J, Zhang Q, et al. Insight into the role of Fe on catalytic performance over the hydrotalcite-derived Ni-based catalysts for CO_2 methanation reaction. Int J Hydrogen Energy 2022;47:7139–49. https://doi.org/10.1016/j.ijhydene.2021.12.057.
[37] Giorgianni G, Mebrahtu C, Schuster ME, Large AI, Held G, Ferrer P, et al. Elucidating the mechanism of the CO_2 methanation reaction over Ni–Fe hydrotalcite-derived catalysts via surface-sensitive in situ XPS and NEXAFS. Phys Chem Chem Phys 2020;22:18788–97. https://doi.org/10.1039/D0CP00622J.
[38] Al Mesfer MK, Danish M, Shah M. Synthesis and optimization of hydrotalcite derived Ni-Fe-Cu based catalysts for catalytic methane decomposition process using the design of experiment approach. J Taiwan Inst Chem Eng 2021;128:370–9. https://doi.org/10.1016/j.jtice.2021.08.045.
[39] He J, Zhang H, Wang W, Yao P, Jiao Y, Wang J, et al. Soot combustion over CeO_2 catalyst: the influence of biodiesel impurities (Na, K, Ca, P) on surface chemical properties. Environ Sci Pollut Res 2021;28:26018–29. https://doi.org/10.1007/s11356-020-11918-2.
[40] Tang Z, Cao H, Tao Y, Heeres HJ, Pescarmona PP. Transfer hydrogenation from glycerol over a Ni-Co/CeO_2 catalyst: a highly efficient and sustainable route to produce lactic acid. Appl Catal B Environ 2020;263:118273. https://doi.org/10.1016/j.apcatb.2019.118273.
[41] Bendieb Aberkane A, Yeste MP, Djazi F, Cauqui MÁ. CO methanation over NiO-CeO_2 mixed-oxide catalysts prepared by a modified co-precipitation method: effect of the preparation pH on the catalytic performance. Nanomaterials 2022;12:2627. https://doi.org/10.3390/nano12152627.
[42] Yoshikawa K, Kaneeda M, Nakamura H. Development of Novel CeO_2-based CO_2 adsorbent and analysis on its CO_2 adsorption and desorption mechanism. Energy Proc 2017;114:2481–7. https://doi.org/10.1016/j.egypro.2017.03.1400.
[43] Qin F, Nohair B, Shen W, Xu H, Kaliaguine S. Promotional effects of CeO_2 on stability and activity of CaO for the glycerolysis of triglycerides. Catal Lett 2016;146:1273–82. https://doi.org/10.1007/s10562-016-1741-6.
[44] Hincapié G, López D, Moreno A. Infrared analysis of methanol adsorption on mixed oxides derived from Mg/Al hydrotalcite catalysts for transesterification reactions. Catal Today 2018;302:277–85. https://doi.org/10.1016/j.cattod.2017.05.052.
[45] Rabiei M, Palevicius A, Monshi A, Nasiri S, Vilkauskas A, Janusas G. Comparing methods for calculating nano crystal size of natural hydroxyapatite using X-ray diffraction. Nanomaterials 2020;10. https://doi.org/10.3390/nano10091627.
[46] Torrente-Murciano L. The importance of particle-support interaction on particle size determination by gas chemisorption. J Nanoparticle Res 2016;18:87. https://doi.org/10.1007/s11051-016-3385-2.
[47] Liu P, Derchi M, Hensen EJM. Promotional effect of transition metal doping on the basicity and activity of calcined hydrotalcite catalysts for glycerol carbonate synthesis. Appl Catal B Environ 2014;144:135–43. https://doi.org/10.1016/j.apcatb.2013.07.010.
[48] Lucrédio AF, Bellido JDA, Assaf EM. Effects of adding La and Ce to hydrotalcite-type Ni/Mg/Al catalyst precursors on ethanol steam reforming reactions. Appl Catal Gen 2010;388:77–85. https://doi.org/10.1016/j.apcata.2010.08.026.
[49] Ashok J, Subrahmanyam M, Venugopal A. Hydrotalcite structure derived Ni–Cu–Al catalysts for the production of H_2 by CH_4 decomposition. Int J Hydrogen Energy 2008;33:2704–13. https://doi.org/10.1016/j.ijhydene.2008.03.028.
[50] Gao J, Wang Y, Ping Y, Hu D, Xu G, Gu F, et al. A thermodynamic analysis of methanation reactions of carbon oxides for the production of synthetic natural gas. RSC Adv 2012;2:2358–68. https://doi.org/10.1039/C2RA00632D.
[51] Schmider D, Maier L, Deutschmann O. Reaction kinetics of CO and CO_2 methanation over nickel. Ind Eng Chem Res 2021;60:5792–805. https://doi.org/10.1021/acs.iecr.1c00389.
[52] Stangeland K, Kalai D, Li H, Yu Z. CO_2 methanation: the effect of catalysts and reaction conditions. Energy Proc 2017;105:2022–7. https://doi.org/10.1016/j.egypro.2017.03.577.
[53] Soubaihi RM, Saoud KM, Dutta J. Comparative investigation of structure and operating parameters on the performance and reaction dynamic of CO conversion on silica aerogel and fumed-silica-supported Pd catalysts. Surface Interfac 2022;29:101776. https://doi.org/10.1016/j.surfin.2022.101776.
[54] Liu Q, Bian B, Fan J, Yang J. Cobalt doped Ni based ordered mesoporous catalysts for CO_2 methanation with enhanced catalytic performance. Int J Hydrogen Energy 2018;43:4893–901. https://doi.org/10.1016/j.ijhydene.2018.01.132.
[55] Ren J, Qin X, Yang JZ, Qin ZF, Guo HL, Lin JY, et al. Methanation of carbon dioxide over Ni-M/ZrO_2 (M = Fe, Co, Cu) catalysts: Effect of addition of a second metal. Fuel Process Technol 2015;137:204–11. https://doi.org/10.1016/j.fuproc.2015.04.022.
[56] Rui N, Zhang X, Zhang F, Liu Z, Cao X, Xie Z, et al. Highly active Ni/CeO_2 catalyst for CO_2 methanation: Preparation and characterization. Appl Catal B Environ 2021;282:119581. https://doi.org/10.1016/j.apcatb.2020.119581.
[57] Tada S, Nagase H, Fujiwara N, Kikuchi R. What are the best active sites for CO_2 methanation over Ni/CeO_2? Energy Fuels 2021;35:5241–51. https://doi.org/10.1021/acs.energyfuels.0c04238.
[58] Khurana D, Dahiya N, Negi S, Bordoloi A, Ali Haider M, Bal R, et al. Improving the coke resistance of Ni-ceria catalysts for partial oxidation of methane to syngas: experimental and computational study. Chem Asian J 2023;18. https://doi.org/10.1002/asia.202201298.
[59] Janz GJ, Wait SC. Space-time yield and reaction rate. J Chem Phys 1955;23:1550–1. https://doi.org/10.1063/1.1742359.
[60] Marín J, Pérez W, Rios L. Low-temperature and highly active nickel catalyst based on hydrotalcite Mg–Al for CO_2 methanation. Energy Technol 2022;10. https://doi.org/10.1002/ente.202200431.